Acta Mechanica Solida Sinica, Vol. 28, No. 4, August, 2015 ISSN 0894-9166
Published by AMSS Press, Wuhan, China

ROCK INITIATION AND PROPAGATION SIMULATION UNDER COMPRESSION-SHEAR LOADING USING CONTINUOUS-DISCONTINUOUS CELLULAR AUTOMATON METHOD**

Fei Yan* **Xiating Feng** **Pengzhi Pan** **Shaojun Li**

(*State Key Laboratory of Geomechanics and Geotechnical Engineering, Institute of Rock and Soil Mechanics, Chinese Academy of Sciences, Wuhan* 430071*, China*)

Received 2 September 2013, revision received 6 May 2015

ABSTRACT A continuous-discontinuous cellular automaton method is developed for rock initiation and propagation simulations, in which the level set method, discontinuous enrichment shape functions and discontinuous cellular automaton are combined. No remeshing is needed for crack growth analysis, and all calculations are restricted to cells without an assembled global stiffness matrix. The frictional contact theory is employed to construct the contact model of normal pressure and tangential shear on crack surfaces. A discontinuous cellular automaton updating rule suitable for frictional contact of rock is proposed simultaneously with Newton's iteration method for nonlinear iteration. Besides, a comprehensive fracturing criterion for brittle rock under compression-shear loading is developed. The accuracy and effectivenesss of the proposed method is proved by numerical simulation.

KEY WORDS continuous-discontinuous cellular automaton method, rock fracturing process, compression-shear loading, frictional contact, comprehensive fracturing criterion

I. INTRODUCTION

Owing to the confining pressure and weight, natural rocks in engineering structures are often under compression and shearing loading. Besides, they are often fraught with joints and cracks. Because of the randomness of joints and fractures of rocks, plus the propagation of those cracks under external loading, failure may occur without the traditional strength theory helping exactly explain the rock strength and rock properties. Tensile failure, shear failure and mixed mode failure are likely to occur in rock engineering under compression and shearing loading. Confronted by the heterogeneity and uncertainty of rocks and the inavailability of the rock failure process, scientists and technicians have never cut down their effort to improve theoretical, experimental, and numerical results. First, for theoretical researches, the initial research on fracture under compression and shearing loading can be found in Griffith's work[1]. Then, Brace[2] and Hoek[3] modified Griffith's brittle fracture theory to account for the effects of crack closure in compression. Later, Cook's research[4] proved that a longitudinal splitting failure would occur when eliminating the friction between the specimen and indenter. Investigations by Lajtai[5], Bazant[6] and Santiago[7] demonstrated that the tensile failure was the main failure mode

* Corresponding author. E-mail: fyan@whrsm.ac.cn; yanfei0324@163.com

** Project supported by the National Key Technologies R & D Program of China (No. 2013BAB02B01) and the National Natural Science Foundation of China (Nos. 41272349, 41172284 and 51322906).

when uniaxial compression had been applied. Blakey[8] believed that the so-called shear failure was actually a secondary phenomenon from the crack propagation process of crack mode I, while the plane of so-called shear failure in compression specimens was actually a plane perpendicular to the maximum tensile stresses.

Secondly, for experimental researches, a large number of rock experiments showed that brittle rock would produce longitudinal cracks parallel to the direction of pressure[9–11]. A solution was checked experimentally by Al-Chalabi and Huang[12] using an epoxy cylindrical specimen with stain gages embedded within and bonded to its surface. Recently, Lee and Jeon[13] studied crack initiation, propagation and coalescence close to pre-existing open cracks in a specimen under uniaxial compression, and Bobet et al.[14,15] studied crack initiation, propagation and coalescence of frictional flaws under uniaxial loads.

Aware of the great importance of criteria for crack initiation and propagation for rocks, many researchers focused on fracture and energy criteria for rocks under compression and shear loading in the past decades. The most common criterion for rock fracture is the maximum circumferential tensile stress, the results by which in agreement with those by experiments[16]. Glucklich[17] and Shen et al.[18] proposed an energy criterion for rock fracture under compression and shear loading, though unsuccessful in distinguishing the effect of tensile stress and compressive stress. Recently, Dobroskok et al.[19] proposed an extended structural criterion for numerical simulation of crack propagation and coalescence under compressive loads, which was an extension of the Neuber-Novozhilov structural fracture propagation criterion, and intended for mode I (tensile) and Mode II (shear) propagation under compressive loads.

Many numerical methods have emerged as useful tools to simulate failure and general behavior of brittle rock fractures, such as FEM, BEM and the meshless method[20]. Firstly, Horii and Nemat-Nasser[21] used singular integral equations to analyze the brittle-ductile transition process, highly accurate as it was, asked for remeshing when airfoil crack began propagating. By combining the damage mechanics approach with a strain-based failure criterion, coalescence through secondary cracks was analyzed by Reyes and Einstein[22]. And Shen and Stephansson[23] combined the discontinuous deformation method(DDM) with a modified G-criterion to simulate the rock fracture propagation. Nemat-Nasser and Horii[24] gave a closed form solution for a regular set of flaws assuming that the pre-existing straight flaws were closed and the trajectory of branching cracks was straight. And Zaitsev and Wittmann[25] studied crack propagation in a specimen with a compressive load but without consideration of the interaction among cracks. Crack propagation, interaction and coalescence for brittle rocks have been studied by Carpinteri et al.[26] within the framework of BEM and DDM, and Han and Swoboda[27] used a damage mechanics model to simulate a set of flaws. Tang et al.[28] combined FEM with damage mechanics and proposed a rock failure process analysis code, while Feng[29] combined FEM, cellular automaton with damage mechanics, and proposed a numerical method of cellular automaton method to analyze rock failure. Recently, Bobet[30] used the code FROCK to model fracture coalescence, and Wu et al.[31] and Steen et al.[32] used the numerical manifold method (NMM) to simulate frictional crack initiation and propagation.

Based on the level set method[33,34], discontinuous enrichment shape functions[33,35] and cellular automaton[36,37], a continuous-discontinuous cellular automaton method (CDCA)[38,39] was proposed by Yan and Feng. In the present work, based on CDCA, a continuous-discontinuous cellular automaton method is developed for rock fracturing process simulations, in which the level set method, discontinuous enrichment shape functions and discontinuous cellular automaton are combined. No remeshing is needed for crack growth. As all calculations are made on cells, so no assembled global stiffness matrix is needed. The frictional contact theory is employed to create a contact model of normal pressure and tangential shear on crack surfaces. A discontinuous cellular automaton updating rule suitable for frictional contact of rocks is proposed simultaneously with Newton's method for nonlinear iteration. In addition, a mixed rock fracturing criterion for brittle rock under compression-shear loading is discussed, and a comprehensive fracturing criterion for brittle rock is developed to overcome the limitations of some other theories, such as defect for shear fracture of the maximum circumferential tensile stress, and insensitivity for tensile stress and compressive stress of the energy criterion, etc. Finally, some numerical results and experimental results are given simultaneously to illustrate the accuracy and efficiency of the present method.

II. CONTINUOUS-DISCONTINUOUS CELLULAR AUTOMATON METHOD

2.1. Crack Tracking

The level set method (LSM)[33,34] is a useful numerical technique for tracking moving interfaces. In the present method, LSM is employed to track the moving interface of a growing crack. In this method, the moving interface of interest is represented as a zero level set function of $\varphi_j(\boldsymbol{x},t)$, which is one dimension higher than the dimension of the interface Γ_j. Then the evolution for the moving interface can be expressed as an evolution of $\varphi_j(\boldsymbol{x},t)$. So discontinuity is independent of grid for calculation . In general, a crack surface can be expressed as a function of $\varphi_j(\boldsymbol{x},t)=0$, which can be seen in Fig.1, and the level set functions of cracks of different shapes can be given as

$$\varphi_j(\boldsymbol{x},t)=\xi(\boldsymbol{x},t)=\begin{cases}\min\limits_{\boldsymbol{x}_{\Gamma_j}\in\Gamma(t)}\left\|\boldsymbol{x}-\boldsymbol{x}_{\Gamma_j}\right\| & (\boldsymbol{x}\in\Omega_1)\\ -\min\limits_{\boldsymbol{x}_{\Gamma_j}\in\Gamma(t)}\left\|\boldsymbol{x}-\boldsymbol{x}_{\Gamma_j}\right\| & (\boldsymbol{x}\in\Omega_2)\end{cases}\qquad\text{for a broken line}\tag{1}$$

$$\varphi_j(\boldsymbol{x},t)=\xi(\boldsymbol{x},t)=\begin{cases}\min\limits_{\boldsymbol{x}_{\Gamma_j}\in\Gamma(t)}(\left\|\boldsymbol{x}-\boldsymbol{x}_{\Gamma_j}\right\|-r_c) & (\boldsymbol{x}\in\Omega_2)\\ -\min\limits_{\boldsymbol{x}_{\Gamma_j}\in\Gamma(t)}(\left\|\boldsymbol{x}-\boldsymbol{x}_{\Gamma_j}\right\|-r_c) & (\boldsymbol{x}\in\Omega_1)\end{cases}\qquad\text{for an arc}\tag{2}$$

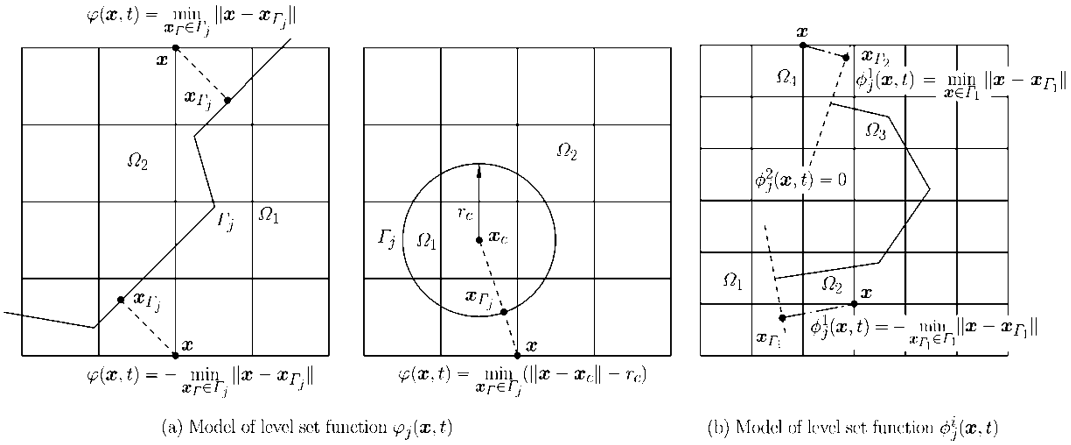

Fig. 1. Discontinuities model and its tracking model.

in which $\boldsymbol{x}$ is the coordinate of a node, and $\boldsymbol{x}_{\Gamma_j}$ is an arbitrary point nearest to point $\boldsymbol{x}$ on the crack surface; Ω_1 and Ω_2 are different domains separated by crack, which can be seen in Fig.1.

The values of the level set functions are stored only at the nodes. The level set functions can be interpolated with the nodal values $\varphi_j^k=\varphi_j^k(\boldsymbol{x}_k,t)$ and known classical finite element shape functions $N_k(\boldsymbol{x})$[33,34].

For an open curve such as a crack, as only one level set function $\varphi_j(\boldsymbol{x},t)$ is not generally sufficient to describe and track the crack, another level set function $\phi_j(\boldsymbol{x},t)$ at crack tip is required. A crack growth in a level set framework is modeled by representing the crack as the zero level set function $\phi_j(\boldsymbol{x},t)$. In this case, two level set functions $\phi_j^1(\boldsymbol{x},t)$ and $\phi_j^2(\boldsymbol{x},t)$ for each tip of crack Γ_j are defined, and the crack tip is represented as the interaction between zero level set function $\varphi_j(\boldsymbol{x},t)$ and the other zero level set function $\phi_j^k(\boldsymbol{x},t)$. So level set functions $\phi_j^1(\boldsymbol{x},t)$ and $\phi_j^2(\boldsymbol{x},t)$ are generally assumed to be orthogonal to $\varphi_j(\boldsymbol{x},t)$[33,34], as given below:

$$\begin{aligned}\phi_j^k(\boldsymbol{x},t)&=\min_{\boldsymbol{x}_{\Gamma_k}\in\Gamma_k}||\boldsymbol{x}-\boldsymbol{x}_{\Gamma_k}|| && (\boldsymbol{x}\in\Omega_1,\boldsymbol{x}\in\Omega_4)\\ \phi_j^k(\boldsymbol{x},t)&=-\min_{\boldsymbol{x}_{\Gamma_k}\in\Gamma_k}||\boldsymbol{x}-\boldsymbol{x}_{\Gamma_k}|| && (\boldsymbol{x}\in\Omega_2,\boldsymbol{x}\in\Omega_3)\end{aligned}\qquad(k=1,2)\tag{3}$$

Like the level set function $\varphi_j(\boldsymbol{x},t)$, the values of $\phi_j^k(\boldsymbol{x},t)$ are stored at the nodes. So the level set functions $\phi_j^k(\boldsymbol{x},t)$ can be interpolated with the nodal values $\phi_j^k(\boldsymbol{x}_m,t)$ and known classical finite element

shape functions $N_m(\boldsymbol{x})$[33,34].

2.2. Frictional Model of Rock Crack Surface

Under compressive loading, crack surfaces in rock may be closed regardless of the existence of normal pressure and tangential friction. Generally, as the normal pressure and tangential friction can influence the propagation mode of crack, the normal pressure and tangential friction of crack surfaces are very important for the crack initiation and propagation process. Consider a crack with two contact surfaces in a rock, as shown in Fig.2, and those two contact surfaces are denoted by Γ_S and Γ_T respectively. The relative displacement between the point $\boldsymbol{x}_S$ on the contact surface Γ_S and the point $\boldsymbol{x}_T$ on another surface Γ_T of crack can be given as Eq.(4)[35], when those two crack surfaces are closed, $\boldsymbol{x}_S$ would coincide with $\boldsymbol{x}_T$, so $\boldsymbol{x}_S$ and $\boldsymbol{x}_T$ are noted as $\boldsymbol{x}$ below:

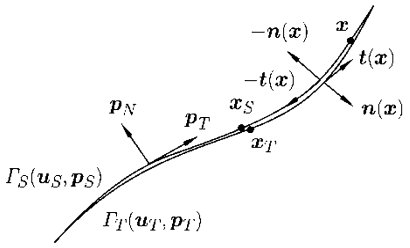

Fig. 2 Crack surface model.

$$g_N(\boldsymbol{x}) = (\boldsymbol{u}_S(\boldsymbol{x}) - \boldsymbol{u}_T(\boldsymbol{x})) \cdot \boldsymbol{n}(\boldsymbol{x}) \tag{4}$$

in which $g_N(\boldsymbol{x})$ is the normal gap between two contact surfaces, $\boldsymbol{u}_S(\boldsymbol{x})$ is the displacement of point $\boldsymbol{x}_S$ on the contact surface Γ_S, and $\boldsymbol{u}_T(\boldsymbol{x})$ is the displacement of point $\boldsymbol{x}_T$ on the contact surface Γ_T, $\boldsymbol{n}(\boldsymbol{x})$ is the unit outward normal vector of point $\boldsymbol{x}$ on contact surface Γ_T, the above symbols can be referred to in Fig.2

For the case of a crack surface being sticky or slippy, we define $\boldsymbol{p}_N$ and $\boldsymbol{p}_T$ as the normal and tangential pressure acting at point $\boldsymbol{x}$, respectively, which can be seen in Fig.2. So the contact condition may be expressed in the standard Kuhn-Tucker form as[35]

$$g_N(\boldsymbol{x}) \geq 0, \qquad \boldsymbol{p}_N \leq 0, \qquad \boldsymbol{p}_N \cdot g_N(\boldsymbol{x}) = 0 \tag{5}$$

In the present method, the penalty method is employed provided penalty factors k_N and k_T are the normal stiffness and shear stiffness, respectively. In the following calculation, we assume that they are constant. According to the contact theory and the penalty method, we assume that the normal load $\boldsymbol{p}_N$ is obtained from multiplication of the penalty factor k_N and the normal gap $g_N(\boldsymbol{x})$. Similarly, the stick component of the tangential load $\boldsymbol{p}_T$ is obtained by multiplying the penalty factor k_T and elastic part of the tangential gap $g_T(\boldsymbol{x})$, and $g_T(\boldsymbol{x})$ is written as

$$g_T(\boldsymbol{x}) = (\boldsymbol{u}_S(\boldsymbol{x}) - \boldsymbol{u}_T(\boldsymbol{x})) \cdot \boldsymbol{t}(\boldsymbol{x}) \tag{6}$$

in which $\boldsymbol{t}(\boldsymbol{x})$ is the unit tangential vector of point $\boldsymbol{x}$ on the contact surface of Γ_T.

Therefore, constitutive laws for the contact pressure can now be summarized as[35]

$$\boldsymbol{p}_N = (\boldsymbol{D}_f^e)_N \boldsymbol{u}^e(\boldsymbol{x}), \qquad \boldsymbol{p}_T = (\boldsymbol{D}_f^e)_T \boldsymbol{u}^e(\boldsymbol{x}) \tag{7}$$

in which $(\boldsymbol{D}_f^e)_N$ and $(\boldsymbol{D}_f^e)_T$ are the normal and tangential parts of the elastic modulus tensor for friction, and $\boldsymbol{u}^e(\boldsymbol{x}) = \boldsymbol{u}_S(\boldsymbol{x}) - \boldsymbol{u}_T(\boldsymbol{x})$ is the relative displacement on point $\boldsymbol{x}$ between crack surfaces Γ_S and Γ_T. The elastic modulus tensor can be written as[35]

$$(\boldsymbol{D}_f^e)_N = -k_N(\boldsymbol{n}(\boldsymbol{x}) \otimes \boldsymbol{n}(\boldsymbol{x})) \tag{8}$$

$$(\boldsymbol{D}_f^e)_T = -k_T(\boldsymbol{I} - \boldsymbol{n}(\boldsymbol{x}) \otimes \boldsymbol{n}(\boldsymbol{x})) \tag{9}$$

The contact surfaces may be sticky or slippy and, based on Coulomb's law and the cohesion contact model, a slip criterion can be given as

$$F_c(\boldsymbol{p}, u) = \|\boldsymbol{p}_T\| - \mu_c \|\boldsymbol{p}_N\| - c_c \begin{cases} = 0 & \text{slip} \\ < 0 & \text{adherence} \end{cases} \tag{10}$$

in which c_c denotes the cohesion between two crack surfaces and Coulomb frictional coefficient is defined as $\mu_c = \tan\varphi_c$, with φ_c denoting the friction angle. In this paper, a trial state/return mapping algorithm is employed to determine the Coulomb friction traction. And a trial function is defined as

$$\phi^{\text{trial}} = ||\boldsymbol{p}_T^{\text{trial}}|| - ||\mu_c \boldsymbol{p}_N|| \tag{11}$$

in which $\boldsymbol{p}_T^{\text{trial}}$ is the trial value of tangential pressure of crack surface. And the algorithm is given as: (1) if $g_N(\boldsymbol{x}) \leq 0$, $\boldsymbol{p}_N = (\boldsymbol{D}_f^e)_N \boldsymbol{u}^e(\boldsymbol{x})$ and $\boldsymbol{p}_T^{\text{trial}} = (\boldsymbol{D}_f^e)_T \boldsymbol{u}^e(\boldsymbol{x})$, and (2) if $\phi^{\text{trial}} \leq 0$ (stick), $\boldsymbol{p}_T = \boldsymbol{p}_T^{\text{trial}}$; otherwise (slip), $\boldsymbol{p}_T = -\mu_c \boldsymbol{p}_N \boldsymbol{p}_T^{\text{trial}} / ||\boldsymbol{p}_T^{\text{trial}}||$.

2.3. Weak Formulation and Integral Equation

Suppose the displacement and traction on each face of the crack surfaces are: $\boldsymbol{w}^S$, $\boldsymbol{t}^S$ on Γ_S and $\boldsymbol{w}^T$, $\boldsymbol{t}^T$ on Γ_T. With reference to both $\boldsymbol{w}^S$ and $\boldsymbol{w}^T$, we use the compact notation $\boldsymbol{w}$, since $\boldsymbol{w}^S$ is always equal to $\boldsymbol{w}^T$. Similarly, $\boldsymbol{t}$ denotes the pair $\boldsymbol{t}^S$ and $\boldsymbol{t}^T$. According to the constitutive law of contact theory, we can get

$$\boldsymbol{t}^S = -\boldsymbol{t}^T, \qquad \boldsymbol{w}^S = \boldsymbol{u}_S, \qquad \boldsymbol{w}^T = \boldsymbol{u}_T \tag{12}$$

According to kinematics, equilibrium, the constitutive laws, and fictional contact theory, the variational formulation can be expressed as[33,35]

$$\int_\Omega \boldsymbol{\sigma} : \nabla^s \boldsymbol{u}^* \mathrm{d}\Omega = \int_\Omega \boldsymbol{b} \cdot \boldsymbol{u}^* \mathrm{d}\Omega + \int_{\Gamma_t} \bar{\boldsymbol{t}} \cdot \boldsymbol{u}^* \mathrm{d}s + \int_{\Gamma_s} \boldsymbol{t} \cdot \boldsymbol{w}^* \mathrm{d}s \tag{13}$$

The superscript * denotes the weight function, which is a mathematical device used for performing a sum, integral, or average to give some elements more 'weight' or influence on the result than the others in the same set. And the last term of Eq.(13) can be rewritten as[33,35]

$$\int_{\Gamma_d} \boldsymbol{t} \cdot \boldsymbol{w}^* \mathrm{d}s = \int_{\Gamma_S} \boldsymbol{t}^S \cdot \boldsymbol{w}^{S^*} \mathrm{d}s + \int_{\Gamma_T} \boldsymbol{t}^T \cdot \boldsymbol{w}^{T^*} \mathrm{d}s = \int_{\Gamma_d} \boldsymbol{t}^S \cdot \tilde{\boldsymbol{u}} \mathrm{d}s \tag{14}$$

in which $\tilde{\boldsymbol{u}} = \boldsymbol{w}^S - \boldsymbol{w}^T$.

In the present method, we use an additional Heaviside function and the exact near-tip asymptotic field functions to enrich the traditional FE shape function. The enriched approximation in modeling the contact surface can be expressed as[33]

$$\begin{aligned} \boldsymbol{u}^h(\boldsymbol{x}) = \sum_{j=1}^{n} N_j(\boldsymbol{x}) u_j + \underbrace{\sum_{k=1}^{m} N_k(\boldsymbol{x}) [H(\varphi(\boldsymbol{x},t)) - H(\varphi(\boldsymbol{x}_k,t))] a_k}_{k \in P} \\ + \underbrace{\sum_{i=1}^{t} N_i(\boldsymbol{x}) \sum_{l=1}^{nf} [F_l(\boldsymbol{x}) - F_l(\boldsymbol{x}_i)] b_i^l}_{i \in T} \end{aligned} \tag{15}$$

in which n and m are the node numbers of elements, and $n = m = 4$ in the present method, as the quadrilateral element is used in the present method. P is the penetrated nodes set, u_j is the regular displacements vector, a_{jk} is a vector of an additional degree of nodal freedom for modeling strong discontinuity t is node number associated with crack tip, and T is crack tip nodes set; nf is the number of the exact near-tip asymptotic field functions; b_i^l is a vector of additional degrees of nodal freedom for modeling the crack tip stress field, and $H(\varphi(\boldsymbol{x}_k,t))$ is the value of $H(\varphi(\boldsymbol{x},t))$ on node $\boldsymbol{x}_k$ and $F_l(\boldsymbol{x}_i)$ is the value of $F_l(\boldsymbol{x})$ on node $\boldsymbol{x}_i$, and $H(\varphi(\boldsymbol{x},t))$ and $F_l(\boldsymbol{x})$ are the Heaviside function and the exact near-tip asymptotic field functions, respectively, which are given as[33]

$$\{F_l(x), l = \text{1-4}\} = \left\{ \sqrt{r} \sin\frac{\theta}{2}, \sqrt{r} \cos\frac{\theta}{2}, \sqrt{r} \sin\theta \sin\frac{\theta}{2}, \sqrt{r} \sin\theta \cos\frac{\theta}{2} \right\} \tag{16}$$

$$H(\varphi(\boldsymbol{x},t)) = \text{sign}(\varphi(\boldsymbol{x},t)) = \begin{cases} 1 & (\forall \varphi(\boldsymbol{x},t) > 0) \\ -1 & (\forall \varphi(\boldsymbol{x},t) < 0) \end{cases} \tag{17}$$

in which r, θ are coordinates of polar coordinates of the crack tip, which can be seen in references by Yan and Feng[38,39].

According to Eq.(15), on crack surface Γ_S and Γ_T, $u_j|_{\Gamma_S} = u_j|_{\Gamma_T}$, $H(\varphi(x,t))|_{\Gamma_S} = 1$, $H(\varphi(x,t))|_{\Gamma_T} = -1$, $F_l(x)|_{\Gamma_S} = \{\sqrt{r}, 0, 0, 0\}$ and $F_l(x)|_{\Gamma_T} = \{-\sqrt{r}, 0, 0, 0\}$ are always satisfied, so we can get the relative

displacement between crack surface Γ_S and Γ_T,

$$\tilde{\boldsymbol{u}} = \boldsymbol{u}_S - \boldsymbol{u}_T = \underbrace{2\sum_{k=1}^{m} N_k(\boldsymbol{x})\boldsymbol{a}_k}_{k\in P} + \underbrace{2\sum_{i=1}^{t} N_i(\boldsymbol{x})\sqrt{r}\boldsymbol{b}_i^0}_{i\in T} = \tilde{\boldsymbol{N}}\{\,\boldsymbol{a}\;\boldsymbol{b}\,\}^{\mathrm{T}} \tag{18}$$

in which $\tilde{\boldsymbol{N}}$ is the shape function which is related to the relative displacement between two crack surfaces, the exact form can be referred as references by Yan and Feng[38].

Substituting Eqs.(15) and (18) into Eqs.(13) and (14), we can obtain

$$\boldsymbol{K}_{ij} = \begin{bmatrix} \boldsymbol{K}_{ij}^{uu} & \boldsymbol{K}_{ij}^{ua} \\ \boldsymbol{K}_{ij}^{au} & \boldsymbol{K}_{ij}^{aa} + \boldsymbol{K}_{ij}^{I} \end{bmatrix}, \qquad \boldsymbol{f}_i = \{\,\boldsymbol{f}_i^u \quad \boldsymbol{f}_i^a - \boldsymbol{f}_i^I\,\} \tag{19}$$

where

$$\boldsymbol{K}_{ij}^{\alpha\beta} = \int_{\Omega^e} (\boldsymbol{B}_i^{\alpha})^{\mathrm{T}} \boldsymbol{D} (\boldsymbol{B}_j^{\beta}) \mathrm{d}\Omega \qquad (\alpha,\beta = u,a) \tag{20}$$

$$\boldsymbol{K}_{ij}^{I} = \int_{\Gamma_S} (\tilde{\boldsymbol{N}}_i)^{\mathrm{T}} (\boldsymbol{D}_f^e) (\tilde{\boldsymbol{N}}_j) \mathrm{d}\Gamma \tag{21}$$

$$\boldsymbol{f}_i^{\alpha} = \int_{\Gamma^e} \boldsymbol{N}_i^{\alpha} \bar{\boldsymbol{t}} d\Gamma + \int_{\Omega^e} \boldsymbol{N}_i^{\alpha} \boldsymbol{f} \mathrm{d}\Omega \qquad (\alpha = u,a) \tag{22}$$

$$\boldsymbol{f}_i^{I} = \int_{\Gamma_S} \tilde{\boldsymbol{N}}^{\mathrm{T}} \boldsymbol{t}_S \mathrm{d}\Gamma \tag{23}$$

in which $\boldsymbol{D}$ is the constitutive matrix of rock, and $\boldsymbol{D}_f^e$ is constitutive matrix contact surfaces which can be referred in Eqs.(8) and (9), N_i^{α} is the traditional finite element shape function, $\boldsymbol{B}_i^{\alpha}$ is a derivative matrix of the traditional finite element shape function matrix.

In Eq.(23), $\boldsymbol{t}_S$ is contact stress of crack surface, which is unknown beforehand in every iteration step, so a Newton's method is applied for the present nonlinear system. Firstly, assuming that

$$\boldsymbol{r} = \begin{Bmatrix} \boldsymbol{f}^u \\ \boldsymbol{f}^a + \boldsymbol{f}^I \end{Bmatrix} - \boldsymbol{K}\boldsymbol{d} = 0 \qquad \boldsymbol{d} = \{\boldsymbol{u},\boldsymbol{a}\}^{\mathrm{T}} \tag{24}$$

in which $\boldsymbol{f}^u = \{\boldsymbol{f}_1^u, \boldsymbol{f}_2^u, \boldsymbol{f}_3^u, \cdots, \boldsymbol{f}_i^u, \cdots, \boldsymbol{f}_m^u\}^{\mathrm{T}}$, $\boldsymbol{f}^{\alpha} = \{\boldsymbol{f}_1^{\alpha}, \boldsymbol{f}_2^{\alpha}, \boldsymbol{f}_3^{\alpha}, \cdots, \boldsymbol{f}_i^{\alpha}, \cdots, \boldsymbol{f}_m^{\alpha}\}^{\mathrm{T}}$ and $\boldsymbol{f}^I = \{\boldsymbol{f}_1^I, \boldsymbol{f}_2^I, \boldsymbol{f}_3^I, \cdots, \boldsymbol{f}_i^I, \cdots, \boldsymbol{f}_m^I\}^{\mathrm{T}}$, and m is the total number of nodes.

According to Newton's method, the nonlinear system of Eq.(24) can be rewritten as

$$\boldsymbol{d}_{n+1} = \boldsymbol{d}_n - \frac{\boldsymbol{r}(\boldsymbol{d}_n)}{\boldsymbol{r}'(\boldsymbol{d}_n)} \tag{25}$$

in which the subscript is the iteration number. First, it is assumed that $\boldsymbol{d}_0 = \{0,0,0,\cdots,0\}^{\mathrm{T}}$ and $\boldsymbol{t}_S = \{0,0\}^{\mathrm{T}}$, then applying Eq.(25), we can get $\boldsymbol{d}_1$, and via $\boldsymbol{d}_1$ we can get contact stress $\boldsymbol{t}_S$, and via $\boldsymbol{d}_1$ and $\boldsymbol{t}_S$ we can get $\boldsymbol{d}_2$ and so on, until $\|\boldsymbol{d}_{n+1} - \boldsymbol{d}_n\| \to 0$.

2.4. Discontinuous Cellular Automaton Theory for Fictional Contact

According to the continuous cellular automaton theory, continuous cellular automaton composed of cell, neighborhood, cell space, cell state and updating rule, and cell state is transferred from one cell to its neighborhood via the updating rule, until cell states of all cells are updated, and convergence is achieved[39]. Based on this theory[38,39], a discontinuous cellular automaton theory is developed, which is composed of cell, crack, neighborhood, crack surface contact state, contact stress, cell space, cell state and discontinuous updating rule, the structure of the discontinuous cellular automaton can be seen in Fig.3(a). Cell state includes cell displacement, cell stress, cell strain, cell force, enriched cell force, enriched cell freedom, crack level set value and crack surface contact state, which can be seen in Fig.3(b). The details of cell, crack and neighborhood can be seen in References[38,39], different from previous continuous cellular automaton, cell state is different, and crack surface contact state and contact stress are new states in the present method. Additionally, the relationship between cell and neighborhood changes with the discontinuity and frictional contact state for the present work, which can be seen in Fig.3(c), Unlike the continuous cellular automaton, the cell stiffness, node force derived from fictional contact is added, Besides, the crack surface contact state and its contact stress must also be considered.

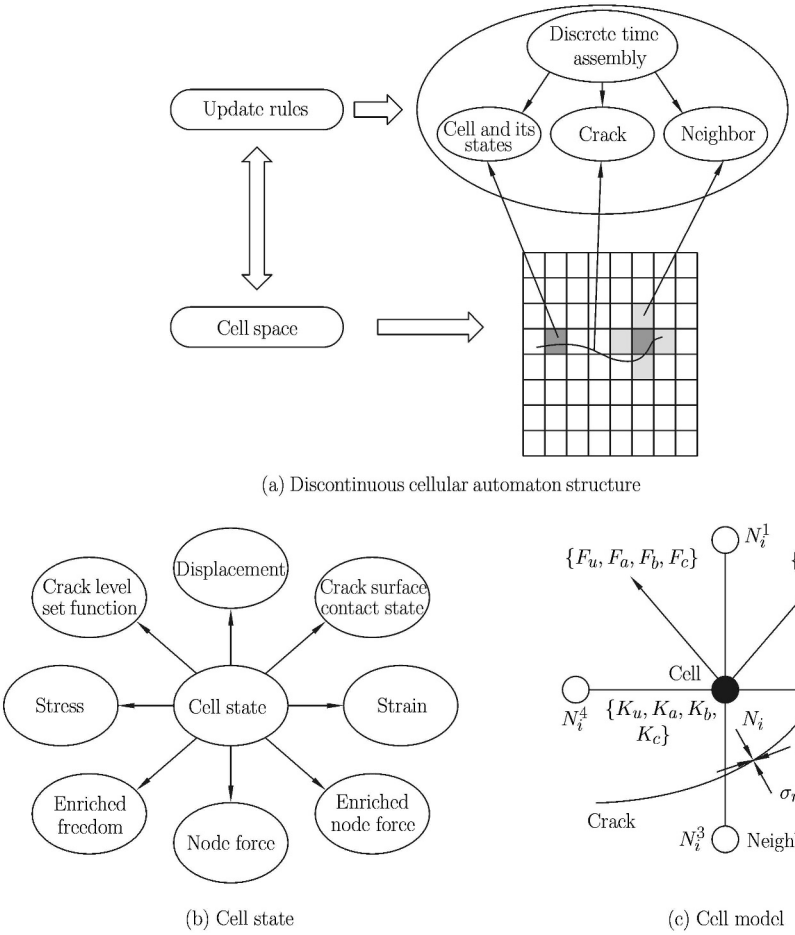

(a) Discontinuous cellular automaton structure

(b) Cell state

(c) Cell model

Fig. 3. Discontinuous cellular automaton model.

2.5. Cellular Automaton Updating Scheme

The discontinuous cellular automaton method (DCA)[38,39] is applied in this method, so the calculation is only focused on cell, and the equilibrium state of the total object can be obtained through the self-organized phenomenon formed by the mutual information transfer between cells. So instead of the global matrix, only cell stiffness is needed in the whole calculation. Secondly, it is easy to consider the local properties of rock element, while the behavior of the cell is thought to be essentially local.

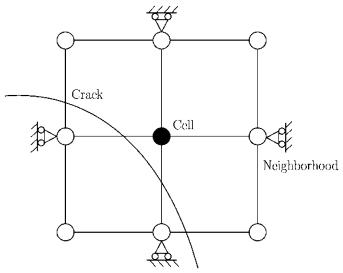

Fig. 4 Cell, neighbors and boundary conditions of updating model.

We assume that the initial state of cell i is $\{\boldsymbol{u}_0, \boldsymbol{f}_0\}^{\mathrm{T}}$, and contact state vector and contact stress are $\boldsymbol{c}_i = \{0, 0\}$ and $\boldsymbol{s}_i = \{0, 0, 0, 0\}$, in which n is the number of total cells which are related to crack contact surfaces. According to Eq.(19), we can get $\boldsymbol{K}_i \triangle \boldsymbol{u}_i = \triangle \boldsymbol{f}_i$. Consider a cellular node N_i with a crack passing through nearby, which can be seen in Fig.4.

As shown in Fig.4, the process of the DCA updating rules is: increment of nodal force leads to the increment of nodal displacement, and the increment of nodal displacement leads the change of cell contact state $\boldsymbol{c}_i$, and the change of cell state leads the increment of cell contact stress $\boldsymbol{s}_i$. The increment of nodal displacement and cell contact stress leads to the increment of nodal force of its neighboring nodes, until the system static equilibrium is achieved. In other words, the self-organization phenomenon of $\triangle \boldsymbol{u}_i^h \to 0$, $\triangle \boldsymbol{f}_i^k \to 0$ appears while cell state $\boldsymbol{c}_i$ remains unchanged. So the updating steps can be given as:

Step (1) According to contact state of last Newton iteration, calculate the cell stiffness matrix $\boldsymbol{K}_i$ and nodal force increment $\triangle \boldsymbol{f}_i$, which includes the contact frictional forces in the last Newton iteration.

Step (2) Restrict all degrees of nodal freedom on all neighboring cells N_i^k, which can be seen in Fig.5.

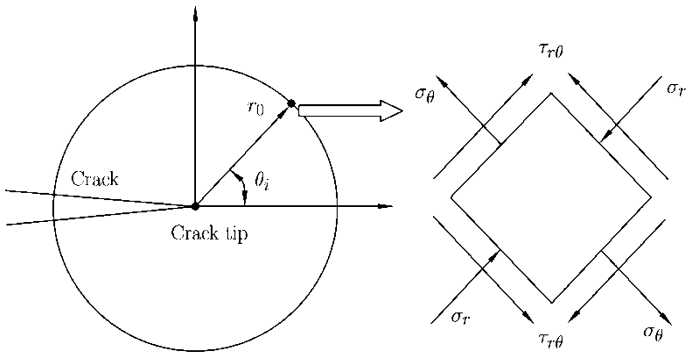

Fig. 5. Stress state of crack tip.

Step (3) Calculate the increment of degrees of nodal freedom $\triangle \boldsymbol{u}_i^h$ via the increment of nodal force $\triangle \boldsymbol{f}_i$ on nodes N_i.

Step (4) updating cell contact state $\boldsymbol{c}_i$ and cell contact stress $\boldsymbol{s}_i$ via the increment of degrees of nodal freedom $\triangle \boldsymbol{u}_i^h$.

Step (5) Obtain the nodal force increment $\triangle \boldsymbol{f}_i^k$ of the neighboring cell N_i^k via $\triangle \boldsymbol{u}_i^h$ from the equation $\triangle \boldsymbol{f}_i^k = \boldsymbol{K}_i^k \triangle \boldsymbol{u}_i^h$, where $\boldsymbol{K}_i^k$ is the stiffness of neighboring cell N_i^k, and if N_i^k is related to the crack surface, the contact frictional forces also needed to be considered.

Step (6) Obtain trial function of crack surface ϕ^{trial} and normal pressure $\boldsymbol{p}_N$ and trial value of tangential pressure $\boldsymbol{p}_T^{\text{trial}}$.

Step (7) if $\phi^{\text{trial}} \leq 0$, stick is occurred, and $\boldsymbol{p}_T = \boldsymbol{p}_T^{\text{trial}}$, then go to step (8); otherwise, slip is occurred, and $\boldsymbol{p}_T = -\mu_c \boldsymbol{p}_N \boldsymbol{p}_T^{\text{trial}} / ||\boldsymbol{p}_T^{\text{trial}}||$, then go back to step (2).

Step (8) Finish the calculation of step (1) - step (5) on all cell nodes, until $\triangle \boldsymbol{u}_i \to 0$ and $\triangle \boldsymbol{f}_i \to 0$ appear.

Step (9) According to step (1) - step (6), calculating iteration residual $\boldsymbol{r}$ of Eq.(24), if $\|\boldsymbol{r}\| <$ toler, iteration finishes, otherwise, updating initial value, cell contact state and cell contact stress and return to step (1).

III. FRACTURE CRITERION FOR BRITTLE ROCK MATERIAL

Although there are many theories for crack propagation prediction, there is no clear evidence of the superiority of one particular criterion over the others. Firstly, there is a big difference between the experimental study with the existing theoretical results for rock fracture under compression and shearing loading. Secondly, many concepts of rock fracture under compression and shearing loading are different from the traditional fracture mechanics, such as: rock under compression may induce a wing crack, and Mode II loading does not always lead to Mode II failure[40]. For example, the maximum circumferential tensile stress criterion is much suitable for predicting Mode I fracture, but unsuitable for shearing fracture mode. Therefore, a mixed fracture criterion has been constructed for tensile fracture and shearing fracture of rocks.

Firstly, a stress state for a crack tip is shown in Fig.5, experiments showing that the crack tip stress distribution characteristics[40], in fact, control the main factors of crack propagation and its properties.

According to the maximum circumferential tensile stress criterion, Mohr-Coulomb criterion and criterion of Bobet and Einstein[30], a modified maximum circumferential tensile stress criterion is proposed. According to the experiment on rock fracture, it is assumed that crack propagation is controlled by the tensile stress and shear stress on an arc whose distance from the crack tip is r_0, which is controlled by the plastic zone of crack tip. Then, we can obtain the criterion as follows:

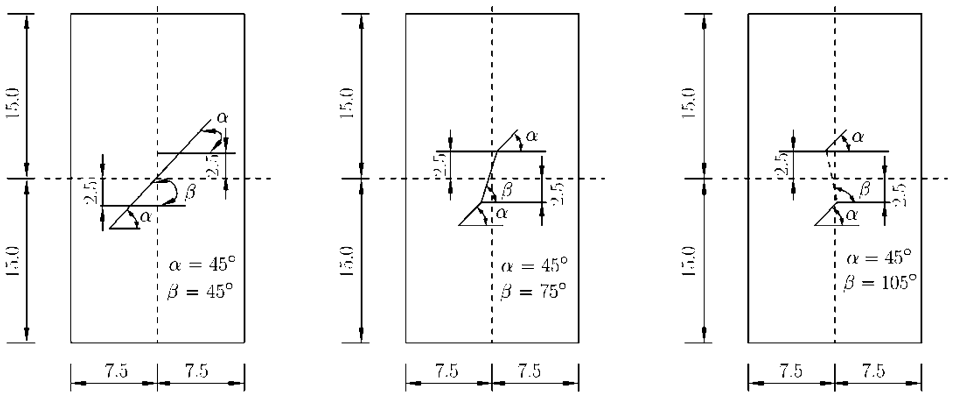

(a) Scheme 1 (b) Scheme 2 (c) Scheme 3

Fig. 6. Specimen and crack models[41].

1. Tensile fracture mode is a top priority. Tensile fracture occurs at $\theta = \theta_0$, and on $\theta = \theta_0$ and $r = r_0$, the tensile stress σ_θ is the maximum, which can be seen in Fig.5, and the tensile stress on this point is equal or greater than the strength $\sigma_{\rm cr}$ of the rock. At this case, when the following conditions are reached, the tensile fracture occurs,

$$[\sigma_\theta(\theta_0, r_0)]_{\max} \geq \sigma_{\rm cr} \tag{26}$$

in which $\sigma_{\rm cr}$ is a critical strength of rock.

2. Shear fracture mode. Shear fracture occurs at an another angle $\theta = \theta_1$, and on $\theta = \theta_1$ and $r = r_0$, the shear stress $\tau_{r\theta}$ is the maximum, which can be seen in Fig.5, and the shear stress on this point satisfies Mohr-Coulomb criterion: $\tau_{r\theta} \geq \sigma_n {\rm tg}\varphi + c$, in which σ_n is the compression on normal direction, and φ is friction angle, c is cohesion of the rock. The conditions for shear fracture are

$$[\tau_{r\theta}(\theta_1, r_0)]_{\max} \geq \sigma_n(\theta_1, r_0){\rm tg}\varphi + c \tag{27}$$

IV. NUMERICAL EXAMPLES

Consider a rock specimen with dimensions 15 mm×30 mm×30 mm in this section, treated as a plane stress problem. There exist two cracks in the specimen, the length of both being 3 mm. Young's modulus of this specimen is $E = 4.78$ GPa, the Poisson's ratio is $\nu = 0.25$, cohesive strength is 15 MPa, and internal friction angle is 49°. Normal stiffness and tangential stiffness of crack surface are given as 200 GPa and 20 GPa. The fracture toughness of $K_{IC} = 1.03$ MPa·m$^{1/2}$, $K_{IIC} = 2.52$ MPa·m$^{1/2}$, and the coefficient of friction of crack surface is given as $\mu_c = 0.50$.

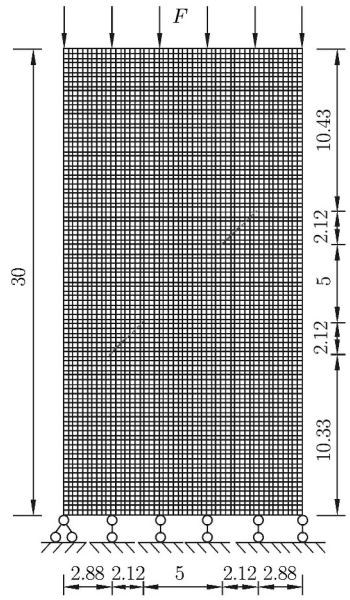

Fig. 7 Mesh grid of rock specimen of CDCA.

The specimen models and position relationship of cracks can be seen in Fig.6[41] and the boundary conditions and loadings are shown in Fig.7. Three cases of different locations of cracks are considered in those examples. Some results of rock fracture experiments are carried out for comparison, which can be seen in Fig.8[41]. Besides, the results by elasto-plastic cellular automaton method (EPCA) are also presented for comparison, which can be seen in Fig.9[41]. Figure 9(a) shows the growing paths results of EPCA for the three schemes, respectively,

and Fig.9(b) shows the growing paths results of scheme 3 for different fracturing steps by EPCA.

The growing paths for two cracks of different locations are shown in Fig.10, in which we can see that the tensile fracture is the main failure mode with uniaxial loading. Compared with the results by EPCA[41] and experiments, an agreement can be achieved between the results of those three methods, and the growing paths of those methods and experiments are almost the same. In those figures, we can see that the growing paths are influenced by the interaction between the cracks when they are getting closer.

Figure 11 plots the propagation process results of scheme 3. Compared with the results of EPCA[41] in Fig.9(b) and experiments, the growing paths of the present method are close to thee other two methods.

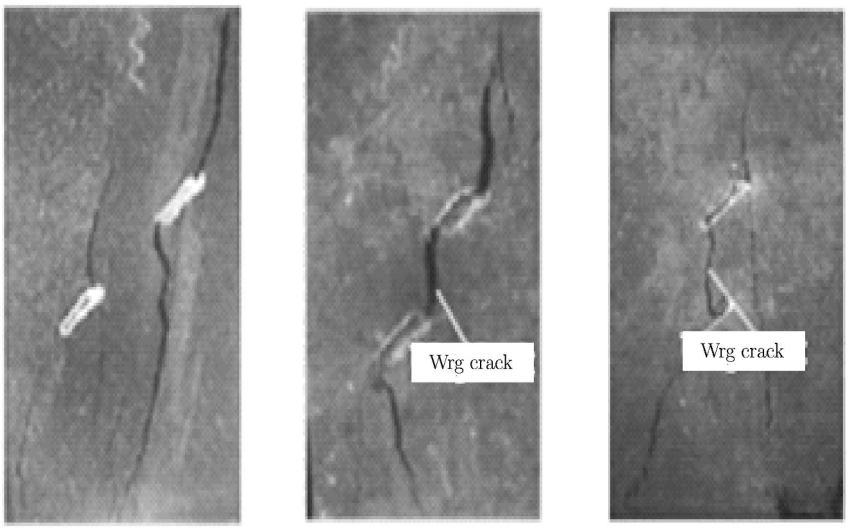

(a) Scheme 1 (b) Scheme 2 (c) Scheme 3

Fig. 8. Experiment results[41].

V. DISCUSSION

Actually, rocks under compression-shear loading may yield different fracture modes, such as mode I, mode II and the mixed mode. So in this section, a rock specimen with a single crack is considered. Firstly, different ratios between confining pressure and axial compression are studied. Secondly, different friction coefficients are considered. Finally, the initial propagating angles of the first step for different cases are discussed.

In this section, a square plate with an inclined crack in its center is considered. The side length of the square is given as 30 cm, and slope angle of crack is 45°, and the other mechanical and physical proprieties are the same as §IV. Different ratios between confining pressure and axial compression and different coefficients of friction μ_c are considered.

5.1. Different Ratios between Confining Pressure and Axial Compression Influences for Fracture Mode

The initial propagating angles of the first step for different value of $P_{\mathrm{H}}/P_{\mathrm{V}}$ are shown in Table 1, and it is shown that the larger the value of $P_{\mathrm{H}}/P_{\mathrm{V}}$, the smaller the angle we can get, which reveals that shear fracture occurs when a much larger value of $P_{\mathrm{H}}/P_{\mathrm{V}}$ is applied.

It is shown in Fig.12 that growing paths change with the ratios between confining pressure and axial compression, in which P_{H} is the confining pressure and P_{V} is the axial compression. According to those figures, we can get the following conclusions,

1. With the increase of the confining pressure, the fracturing paths under biaxial stress gradually becomes parallel to the initial crack direction.

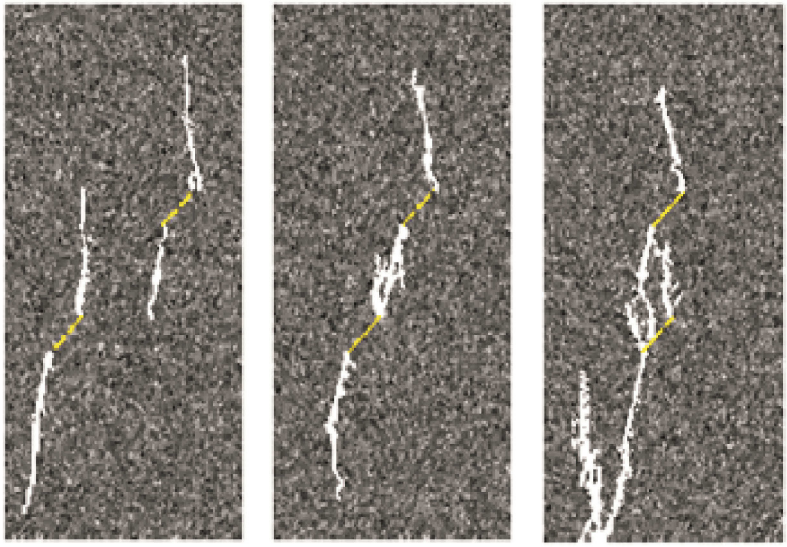

a. Scheme 1 b. Scheme 2 c. Scheme 3

(a) Fracturing process by EPCA[41]

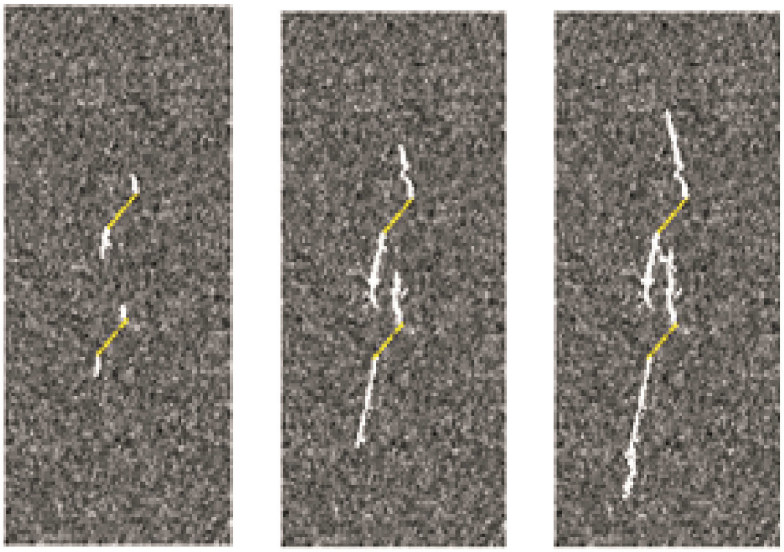

(b) Fracturing process of Scheme 3 by EPCA[41]

Fig. 9. Rock fracturing process results by EPCA.

Table 1. **The initial propagation angles for different values of $P_{\mathrm{H}}/P_{\mathrm{V}}$**

$P_{\mathrm{H}}/P_{\mathrm{V}}$	0.1	0.2	0.3
Initial propagation angle	78.12	58.95	32.87

2. The growing paths change from curve to straight line with the increasing of the confining pressure.

3. The fracture mode gradually changes from tensile fracture mode to shear fracture mode with the increase of confining pressure, actually, when tensile fracture occurs, the initial propagating direction deviates from the extension direction of the crack, otherwise, when shear fracture occurs, the initial propagating direction is the extending direction of the crack.

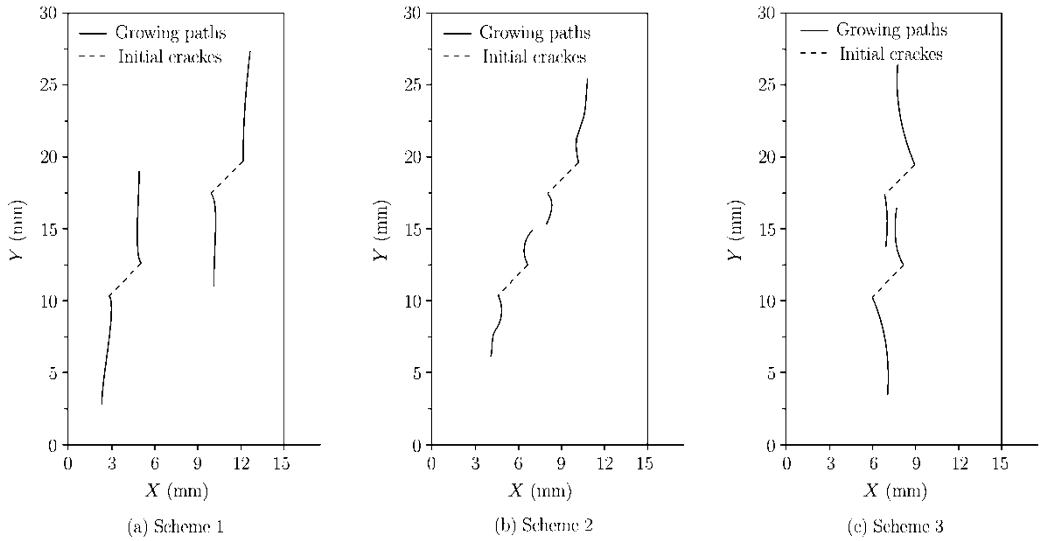

Fig. 10. Fracturing process by CDCA.

5.2. Different Coefficients of Friction Influences for Fracture Mode

The initial propagating angles of the first step for different values of coefficients of friction on crack surfaces μ_c are shown in Table 2. It can be seen from this table that a small angle can be obtained when the coefficients of friction on crack surfaces μ_c get larger, which reveal that shear fracture occurs when a much larger value of μ_c is applied.

Table 2. **The initial propagation angles for different values of coefficients of friction**

Coefficients of friction	$\mu = 0.32$	$\mu = 0.48$	$\mu = 0.67$	$\mu = 0.83$
Initial propagation angle	82.05	47.97	25.13	13.52

It is shown in Fig.13 that plots the fracture paths under different values of coefficients of friction on crack surfaces μ_c, in which a biaxial stress is applied, and $P_{\mathrm{H}}/P_{\mathrm{V}} = 0.2$. From those figures, we can conclude,

1. As the coefficient of friction μ_c increases, the fracturing paths gradually get close to parallel to the initial crack direction.

2. The growing paths change from curve to straight line with an increase of the coefficients of friction μ_c.

3. The fracture mode gradually changes from tensile fracture mode to shear fracture mode with the increase of the coefficients of friction μ_c. In fact, when tensile fracture occurs, the initial propagating direction deviates from the propagation direction of the crack, otherwise, when shear fracture occurs, the initial propagating direction is the extending direction of the crack.

VI. CONCLUSION

In this work, a continuous-discontinuous cellular automaton method (CDCA) is developed for fracturing process simulation of brittle rocks under compression-shear loading. Firstly, the level set method, discontinuous enrichment shape functions and discontinuous cellular automaton are combined, and a CDCA is proposed. No remeshing is needed for crack propagation analysis. The calculation of the present method is restricted to cells and, according to the updating rules and cell intersection, information on one cell can be transferred into all the rest So no assembled global stiffness matrix is needed in the whole calculation. And the frictional contact theory for rock material has been employed, by which a contact model of normal pressure and tangential shear on crack surfaces under compression-shear loading is constructed. Finally, a mixed rock fracturing criterion for brittle rocks under compression-shear loading

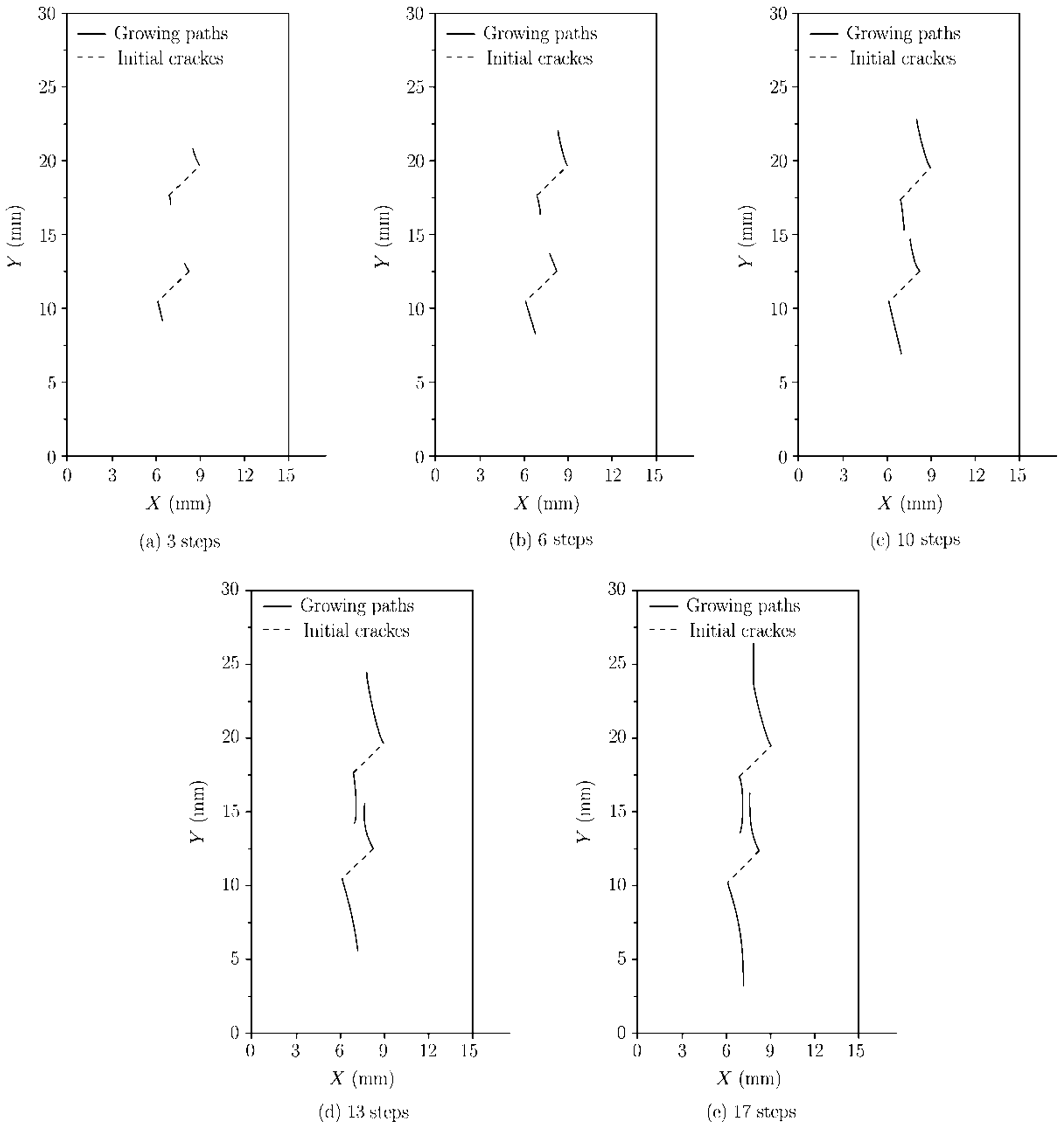

Fig. 11. Fracturing process of Shceme 3 by CDCA.

is discussed. Based on the criterion of Bobet and Einstein, a comprehensive fracturing criterion for brittle rocks is developed along with the following conclusions.

1. It is shown that agreement can be achieved between the results by the present method and those by EPCA and rock experiments. So the present method is effective and can be widely used in engineering practice.

2. Numerical examples show that the mixed rock fracturing criterion for brittle rock, which is developed from the criterion of Bobet and Einstein in the present method, is effective. Specifically, different loadings and friction coefficients lead to different initial propagating angles, which agrees with experimental results.

3. Numerical examples have verified that different friction coefficients and ratios between confining pressure and axial compression may lead to different fracturing modes. And the fracture paths for different friction coefficients and ratios between confining pressure and axial compression are also different.

References

[1] Griffith,A.A., The phenomena of rapture and flow in solids. *Philosophical Transactions of the Royal Society A*, 1921, 221: 163-197.

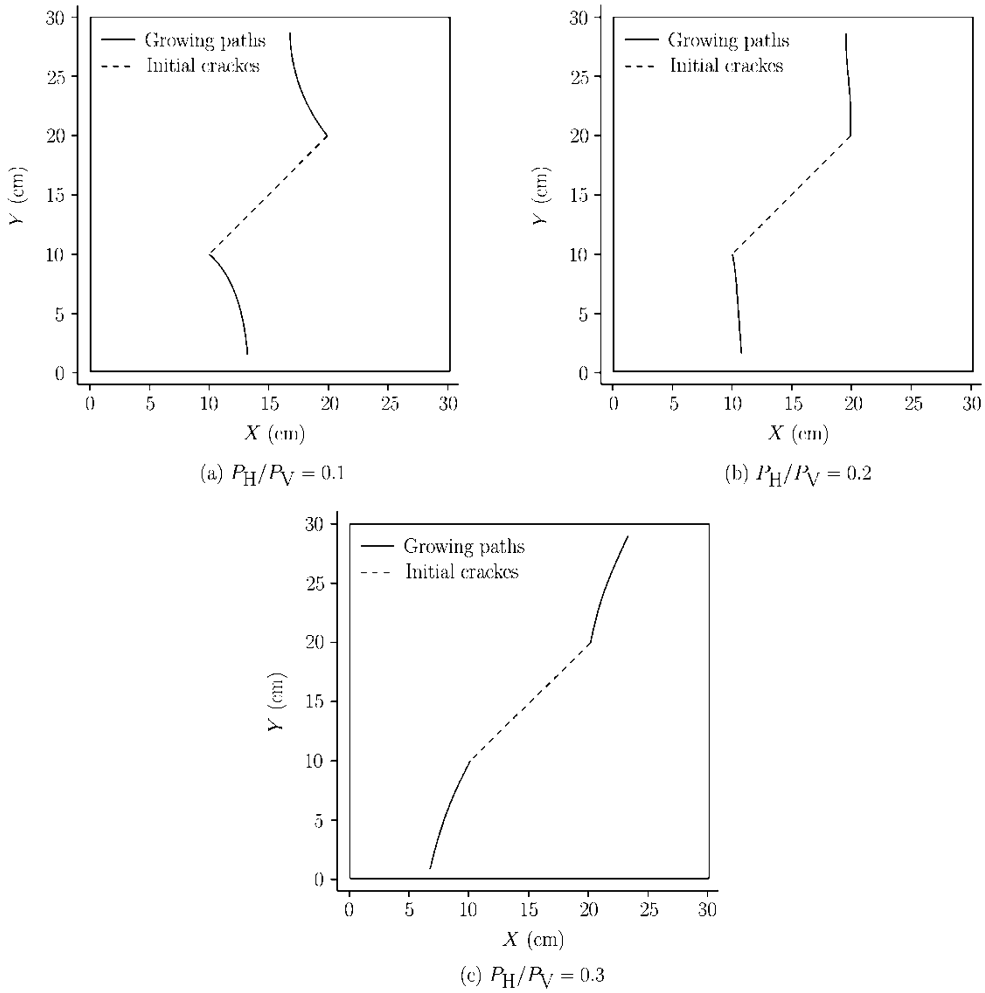

Fig. 12. Fracture path on different values of P_H/P_V.

[2] Brace,W.F., Brittle fracture of rocks. In: State of Stress in the Earth's Crust. (ed Judd). New York, U.S.A.: American Elsevier Publishing Co, 1964: 111-180.

[3] Hoek,E. and Bieniawski,Z.T., Application of the photoelastic coating technique to the study of the stress redistribution associated with plastic flow around notches. *The South African Institution of Mechanical Engineering*, 1963, 12(8): 222-226.

[4] Jaeger,G.C. and Cook,N.G.W., Foundamental of rock mechanics (2^{nd} Edn). London, U.K.: Chapman and Hall, 1976: 20-55.

[5] Lajtai,E.Z., A theoretical and experimental evaluation of Griffith theory of brittle fracture. *Techonophysics*, 1971, 11: 129-156.

[6]] Bazant,Z.P., Crack band theory for fracture of concrete. *Materials and Structures*, 1983, 16: 155-177.

[7] Santiago,S.D. and Hilsdorf,H.K., Fracture mechanism of concrete under compressive loads. *Cement and Concrete Research*, 1973, 3: 363-388.

[8] Blakey,F.A., Mechanism of fracture of concrete. *Nature*, 1952, 170: 1120.

[9] Hawkes,I. and Mellor,M., Uniaxial testing in rock mechanics laboratories. *Engineering Geology*, 1970, 4: 177-285.

[10] Chsu,T.T., Slate,G.M., Sturman,G.M. and Winter,G., Microcracking of plain concrete and the shape of the stress-strain curve. *ACI Journal proceeding*, 1963, 60: 209-224.

[11] Peng,S.D. and Johnson,A.M., Crack growth and faulting in cylindrical specimens of chelmsford granite. *International Journal of Rock Mechanics and Mining Sciences & Geomechanics*, 1972, 9: 37-86.

[12] Al-Chalabi,M. and Huang,C.L., Stress discontribution within circular cylinders in compression. *International Journal of Rock Mechanics and Mining Sciences & Geomechanics*, 1974, 11: 45-56.

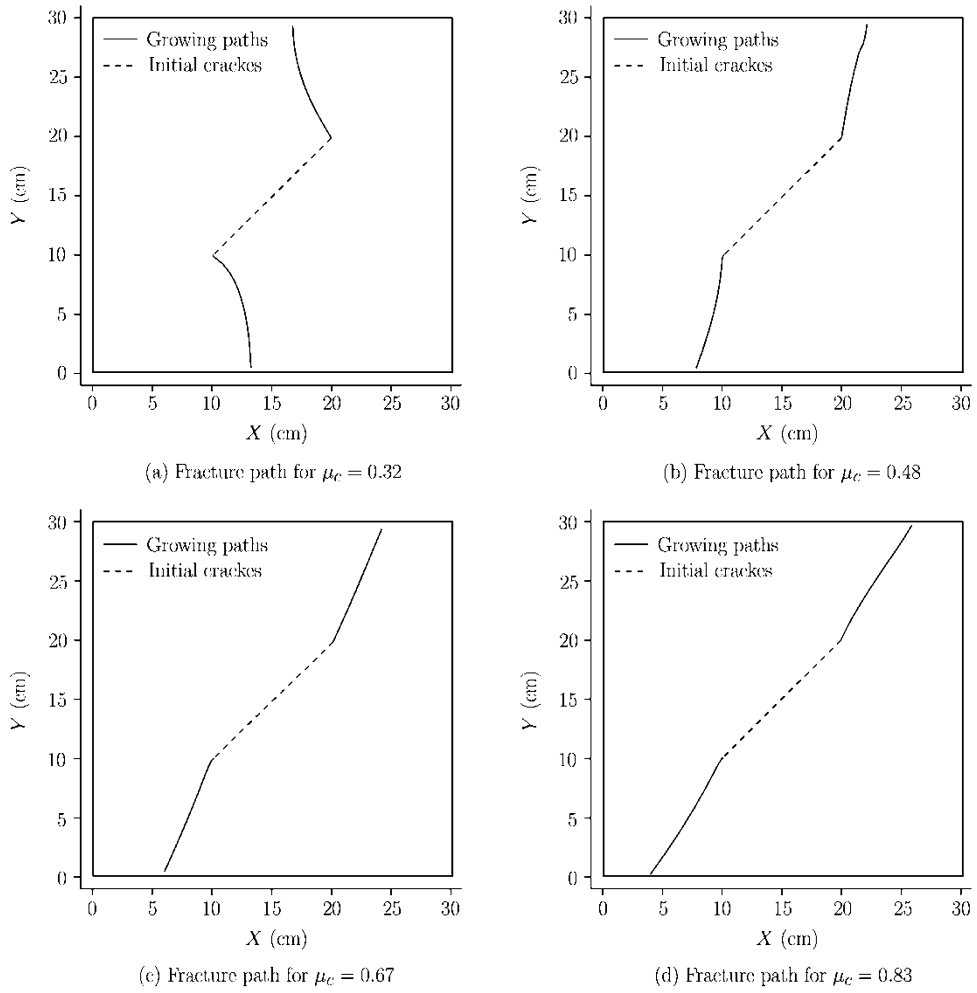

Fig. 13. Fracture path on different values of coefficients of friction.

[13] Lee,H. and Jeon,S., An experimental and numerical study of fracture coalescence in pre-cracked specimens under uniaxial compression. *International Journal of Solids and Structures*, 2011, 48: 979-999.

[14] Park,C.H. and Bobet,A., Crack initiation, propagation and coalescence from frictional flaws in uniaxial compression. *Engineering Fracture Mechanics*, 2010, 77: 2727-2748.

[15] Sagong,M. and Bobet,A., Coalescence of multiple flaws in a rock-model material in uniaxial compression. *International Journal of Rock Mechanics and Mining Science*, 2002, 39: 229-241.

[16] Sih,G.C., Some basic problems in fracture mechanics and new concepts. *Journal of Engineering Fracture*, 1973, 5: 365-377.

[17] Glucklich, Fracture of plain concrete. *Journal of Engineering Mechanics*, 1963, 89: 127-138.

[18] Shen,B. and Stephansson,O., Numerical analysis of mixed mode I and II fracture propagation. *International Journal of Rock Mechanics and Mining Sciences & Geomechanics Abstracts*, 1993, 30: 861-867.

[19] Dobroskok,A., Ghassemi,A. and Linkov,A., Extended structural criterion for numerical simulation of crack propagation and coalescence under compressive loads. *International Journal of Fracture*, 2005, 133: 223-246.

[20] Miao,Y., He,T.G., Yang,Q. and Zheng,J.J., Multi-domain hybrid boundary node method for evaluating top-down crack in asphalt pavements. *Engineering Analysis for Boundary Elements*, 2010, 34(9): 755-760.

[21] Horii,H. and Nemat-Nasser,S., Brittle failure in compression splitting, faulting and brittle-ductile transition. *Philosophical Transactions of the Royal Society A*, 1986, 319: 337-374.

[22] Reyes,O. and Einstein,H.H., Failure mechanisms of fractured rock—a fracture coalescence model. In 7th Int. Congress on Rock Mech., 1, ed. Balkema: Wittke W. Rotterdam, 1991, 333-340.

[23] Shen,B. and Stephansson,O., Modification of the G-criterion for fracture propagation subjected to compression. *International Journal of Rock Mechanics and Mining Science*, 1993, 30: 681-687.

[24] Nemat-Nasser,S. and Horii,H., Compression-induced non-planar crack extension with application to splitting, exfoliation and rockbursts. *Journal of Geophysical Research*, 1982, B87: 6805-6821.
[25] Zaitsev,Y.V. and Wittmann,F.H., Simulation of crack propagation and failure of concrete. *Materials and Structures*, 1981, 14: 357-365.
[26] Carpinteri,A., Scavia,C. and Yang,G.P., Microcrack propagation, coalescence and size effects in compression. *Engineering Fracture Mechanics*, 1996, 54(3): 335-347.
[27] Han,B.C. and Swobada,G.A., A damage mechanics model with wing cracks propagation. In: Computer Methods and Advances in Geomechanics, 2, eds. Siriwardane HJ, Zaman MM. Balkema: Rotterdam, 1993: 1555-1559.
[28] Tang,C.A. and Kou,S.Q., Crack propagation and coalescence in brittle materials under compression. *Engineering Fracture Mechanics*, 1998, 61: 311-324.
[29] Feng,X.T., Pan,P.Z. and Zhou,H., Simulation of the crack microfracturing process under uniaxial compression using an elasto-plastic cellular automaton. *International Journal of Rock Mechanics and Mining Science*, 2006, 43: 1091-1108.
[30] Bobet,A. and Einstein,H.H., Numerical modeling of fracture coalescence in a model rock material. *International Journal of Fracture*, 1998, 92: 221-252.
[31] Wu,Z.J. and Wong,L.N.Y., Frictional crack initiation and propagation analysis using the numerical manifold method. *Computers and Geotechnics*, 2012, 39: 38-53.
[32] Steen,B.V., Vervoort,A. and Napier,J.A.L., Numerical modeling of fracture initiation and propagation in biaxial tests on rock samples. *International Journal of Fracture*, 2001, 108: 165-191.
[33] Stolarska,M., Chopp,D.L., Moes,N. and Belytschko,T., Modelling crack growth by level sets in the extended finite element method. *International Journal for Numerical Methods in Engineering*, 2001, 51: 943-960.
[34] Sethian,J., Evolution, implementation and application of level set and fast marching methods for advancing fronts. *Journal of Computational Physics*, 2001, 169: 503-555.
[35] Moes,N. and Belytschko,T., Extended finite element method for cohesive crack growth. *Engineering Fracture Mechanics*, 2002, 69: 813-833.
[36] Shen,C., Dai,S., Yang,J. and Tang,X., Cellular automata for analysis of plane problem in theory of elasticity. *Journal of Tsinghua University (Science & Technology)*, 2001, 41: 35-38 (in Chinese).
[37] Gurdal,Z. and Tatting,T., Cellular automata for design of truss structures with linear and non-linear response. In: Proceedings of 41st AIAA/ASME/ASCE/AHS/ASC Structural Dynamics and Materials Conference, GA: Atlanta, 2000.
[38] Pan,P.Z., Yan,F. and Feng,X.T., Modeling the cracking process of rocks from continuity to discontinuity using a cellular automaton. *Computers and Geosciences*, 2012, 42: 87-99.
[39] Yan,F., Feng,X.T., Pan,P.Z. and Li,Y.P., A continuous-discontinuous cellular automaton method for regular frictional contact problems. *Archive of applied mechanics*, 2013, 83(8): 1239-1255.
[40] Rao,Q.H., Sun,Z.Q., Stephansson,O., et al., Shear fracture (Mode II) of brittle rock. *International Journal of Rock Mechanics and Mining Science*, 2003, 40: 355-375.
[41] Pan,P.Z., Ding,W.X., Feng,X.T., et al., Research on influence of pre-existing crack geometrical and material properties on crack propagation in rocks. *Chinese Journal of Rock Mechanics and Engineering*, 2008, 27(9): 1882-1889.